Supplement of Geosci. Model Dev., 17, 9023–9049, 2024
https://doi.org/10.5194/gmd-17-9023-2024-supplement

Geoscientific Model Development
Open Access
EGU

Supplement of

Reconciling surface deflections from simulations of global mantle convection

Conor P. B. O'Malley et al.

Correspondence to: Gareth G. Roberts (gareth.roberts@imperial.ac.uk)

Contents of this file

1. Figures S1 to S19.

S1 Introduction

This document includes nineteen figures in three groups. First, Figures S1–S2 summarise the setup of the numerical simulations, and show examples of results and resultant surface deflections. They expand upon the results shown in Figures 1–2 in the main manuscript. Secondly, Figures S3–S7 show surface deflections and sensitivity kernels calculated by solving the equations of motion analytically using the propagator matrix approach and associated statistics. They show results for models that include self-consistent radial gravitation and removal of shallow structure, expanding upon the results shown in Figures 3–5 in the main manuscript. Figures S8–S14 show calculated vertical surface deflections from models in which viscosity and density are modified. These figures includes comparisons of surface deflections calculated using the different approaches (numeric and analytic) and model parametrizations. They extend the results shown in Figures 7–8 in the main manuscript. Figures S15–S19 show effective contributions from density anomalies in the mantle to instantaneous surface deflections. In the main text, we show spherical harmonic solutions up to a maximum spherical harmonic degree $l = 50$ (see Figure 9 in the main manuscript). Here, results are presented for maximum degrees 40, 30, 20, 10 and 5. The results demonstrate the importance of contributions from short wavelength (high degree) density structure to surface deflections, especially at shallow depths.

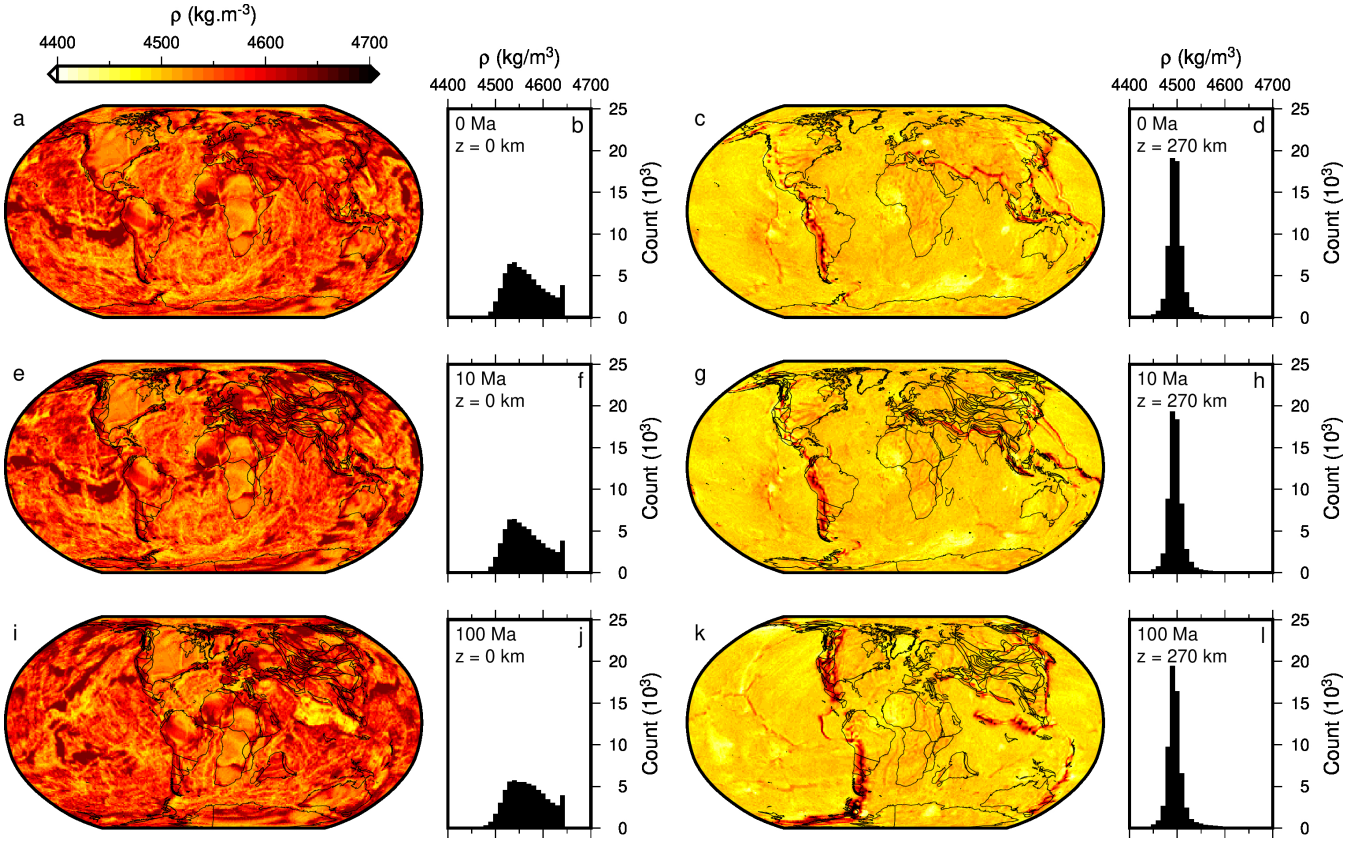

Figure S1. Model 1: Densities predicted from numerical simulation of mantle convection. (a) Predicted present-day density ρ, at surface (z=0), from TERRA model with viscosity independent of temperature (Model 1a), plotted at grid resolution of 1 degree. (b) Histogram of values shown in (a), weighted by latitude to correct to equal-area. (c–d) As (a–b) but for densities at a depth of 270 km. (e–h) As (a–d) but for time slice at 10 Ma; paleo-coastlines generated from Phanerozoic plate rotation history of Merdith et al. (2021). (i–l) As (a–d) but for time slice at 100 Ma.

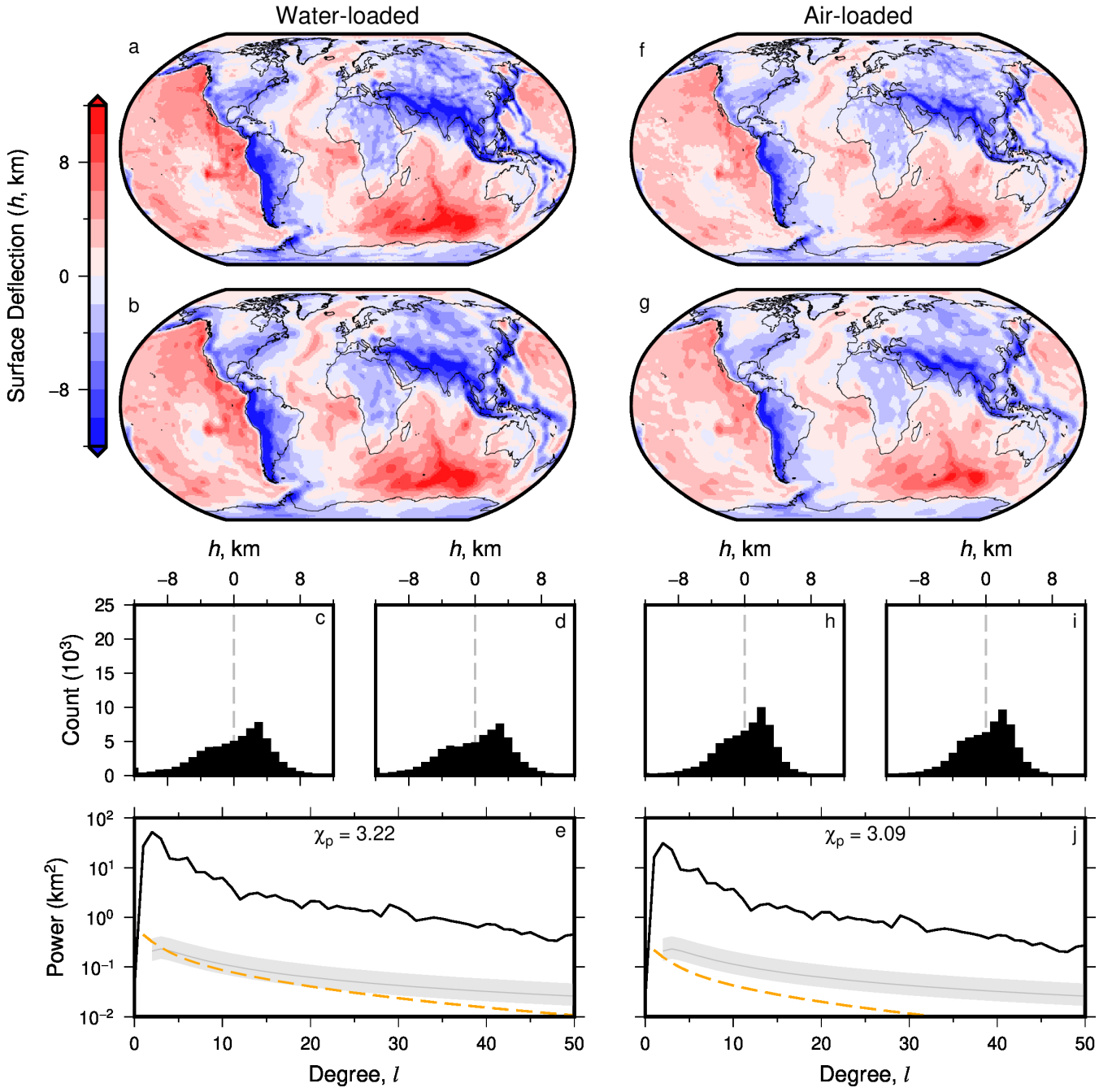
Water-loaded
Air-loaded
a
b
c
d
e
f
g
h
i
j
Surface Deflection (h, km)
8
0
−8
h, km
−8
0
8
Count (10³)
25
20
15
10
5
0
Power (km²)
10²
10¹
10⁰
10⁻¹
10⁻²
χp = 3.22
χp = 3.09
0
10
20
30
40
50
Degree, l

Figure S2. Model 1: Predicted water- and air-loaded surface deflections. (a) Water-loaded, present day, surface deflection predicted by Model 1a. Figure S2a shows normal stress, σ, used with Equation 2 in the main manuscript to calculate surface deflections, h; ρ_w = 1030 kg m^{-3}. (b) Spherical harmonic fit (Model 1b) up to degree l = 50 of grid shown in (a), calculated using the approach of Hoggard et al. (2016). (c–d) Histogram of values shown in (a) and (b) respectively, weighted by latitude to correct to equal-area. (e) Black line = power spectrum in terms of total power per degree, from spherical harmonic expansion shown in (b); gray line and band = expected dynamic topography from Kaula's rule using admittance $Z = 12 \pm 3$ mGal km^{-1} (Kaula, 1963). Orange dashed line = expected power spectrum for water-loaded residual topography from Holdt et al. (2022) via analytical solution of special case of Equation 4 of the main manuscript. χ_p = total root-mean-squared difference between distribution of modeled and theoretical surface deflection power (see Equation 9 in the main manuscript). (f–j) As (a–e) but for air-loaded surface deflection; ρ_w = 1 kg m^{-3}.

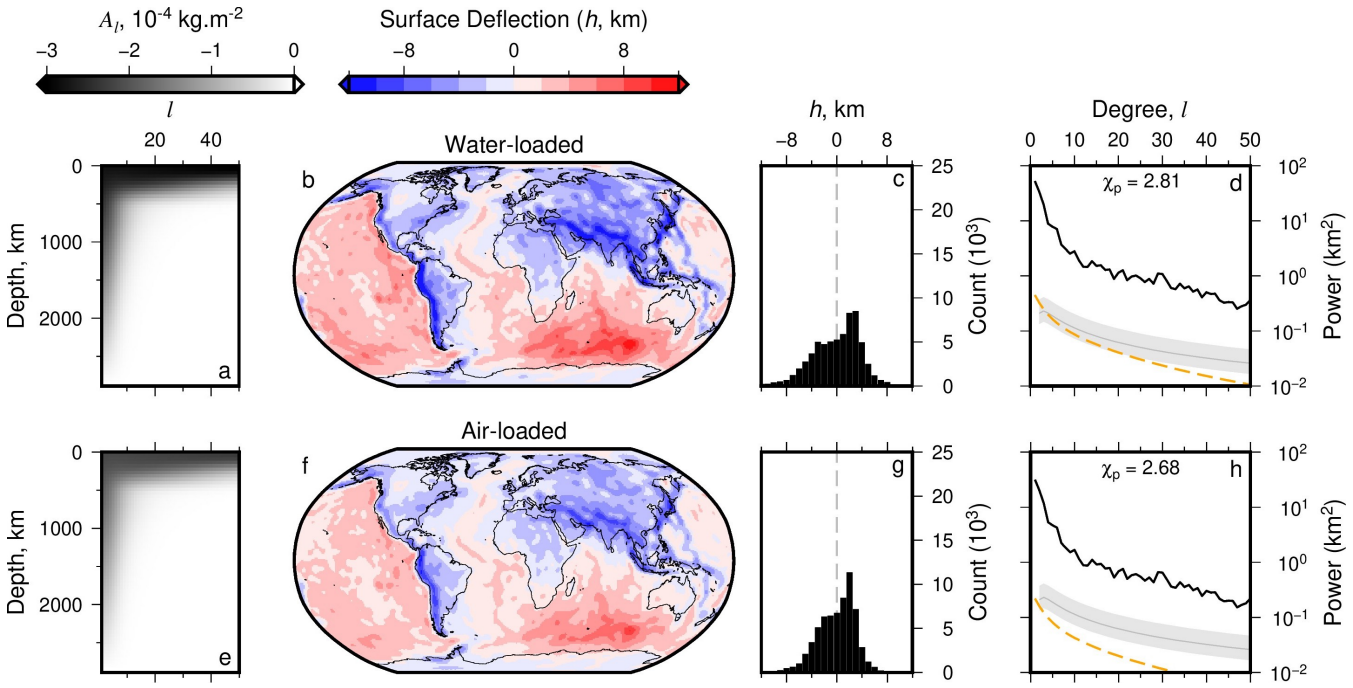

Figure S3. Model 2: Propagator matrix solution for surface deflection with associated sensitivity kernels. (a) Surface deflection sensitivity kernel A_l, as a function of spherical harmonic degree, l, and depth, calculated for the radial viscosity structure (and other parameters) which were used to generate Model 1; see Equation 5 in the main manuscript. (b) Present-day predicted water-loaded surface deflection, calculated using propagator matrix method, from spherical harmonic expansion (to maximum degree l = 50) of density structure (e.g., Figure S1) and radial viscosity structure (e.g., Figure 2c; Corrieu et al., 1995; Hager et al., 1985; Parsons & Daly, 1983). Note that for comparison with numeric calculations shown in Figure 3, no terms related to flow-related perturbation of gravitational potential terms are included (see Equations 5 and 6 in the main manuscript), and gravitational acceleration $g = 10$ m s^{-2} everywhere. (c) Histogram of values shown in (b), weighted by latitude to correct to equal-area. (d) Black line = power spectrum in terms of total power per degree, from surface deflection prediction shown in (a); gray line and band = expected dynamic topography from Kaula's rule using admittance $Z = 12 \pm 3$ mGal km^{-1} (Kaula, 1963). Orange dashed line = power spectrum of water-loaded residual topography from Holdt et al. (2022), via analytical solution of special case of Equation 4 in the main manuscript. χ_p = total root-mean-squared difference between distribution of modeled and theoretical surface deflection power (see Equation 9 in the main manuscript). (e–h) As (a–d) but for air-loaded surface deflection; ρ_w = 1 kg m^{-3}.

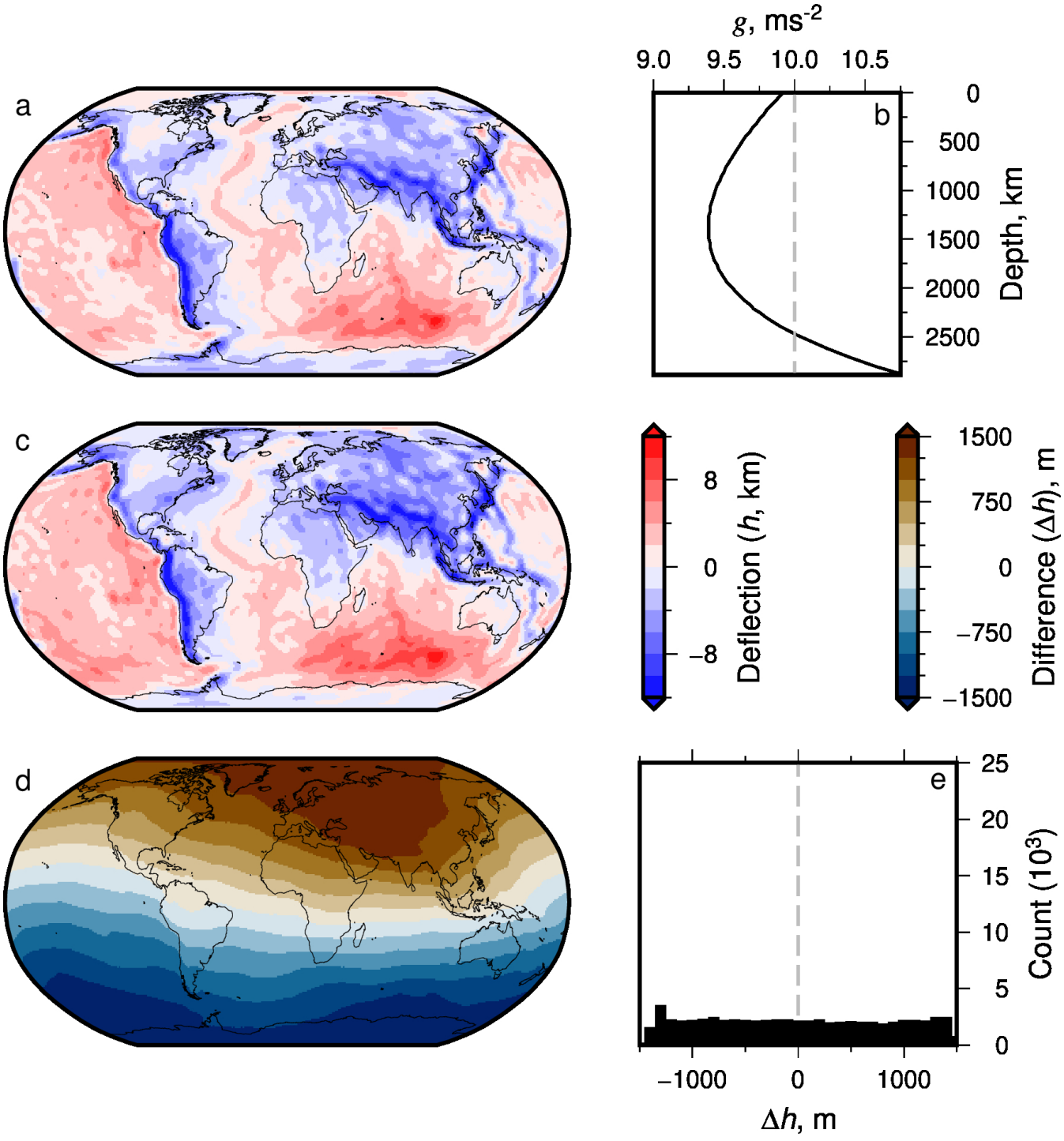
a
b
c
d
e
g, ms-2
9.0
9.5
10.0
10.5
0
500
1000
1500
2000
2500
Depth, km
8
0
−8
Deflection (h, km)
1500
750
0
−750
−1500
Difference (Δh), m
25
20
15
10
5
0
Count (10³)
−1000
0
1000
Δh, m

Figure S4. Model 3: Predicted surface deflection from mantle convection in presence of radial gravitation. (a) Predicted present-day water-loaded surface deflection calculated using propagator matrix method, incorporating radial gravitation i.e., $g(r)$, black curve in (b).(b) Black curve = profile of gravitational acceleration as a function of radius, given density distribution predicted by Model 1a; gray dashed line = constant value of g = 10 m s^{-2} used within TERRA model runs and in previous figures. (c) As (a) but calculated using g = 10 m s^{-2} everywhere, i.e., same as Figure S3a–d (see dashed line in panel b). Associated sensitivity kernels are shown in Figure S6. (d) Difference between surface deflections predicted by Models 3 and 2 (panels a and c). (e) Histogram of values in (d), weighted by latitude to correct to equal-area.

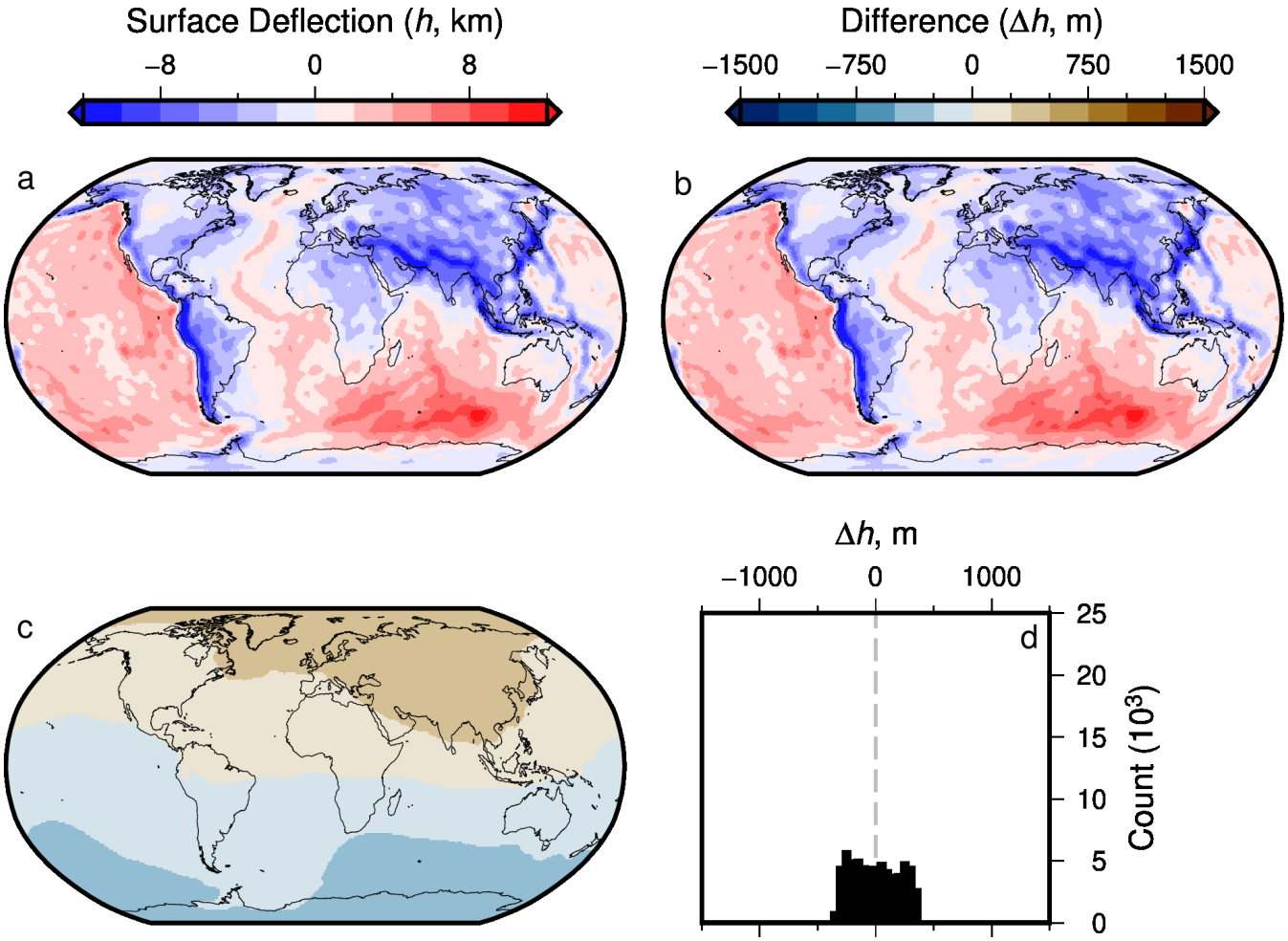

Figure S5. Model 4: Comparing predicted surface deflections with and without stress perturbations induced by gravitational potential of deflected surface. (a) Predicted present-day water-loaded surface deflection calculated using propagator matrix method, with g = 10 m s^{-2} everywhere, including terms describing stress perturbation due to change in gravitational potential (i.e., u_3 term in Equation 5 in the main manuscript). (b) As (a) but calculated excluding u_3 term, i.e., same as Figure S3a. See Figure S6 for associated sensitivity kernels. (c) Difference between Models 4 and 2 (panels a and b). Note same colour scales are used as in Figure S4. (d) Histogram of values in (d), weighted by latitude to correct to equal-area.

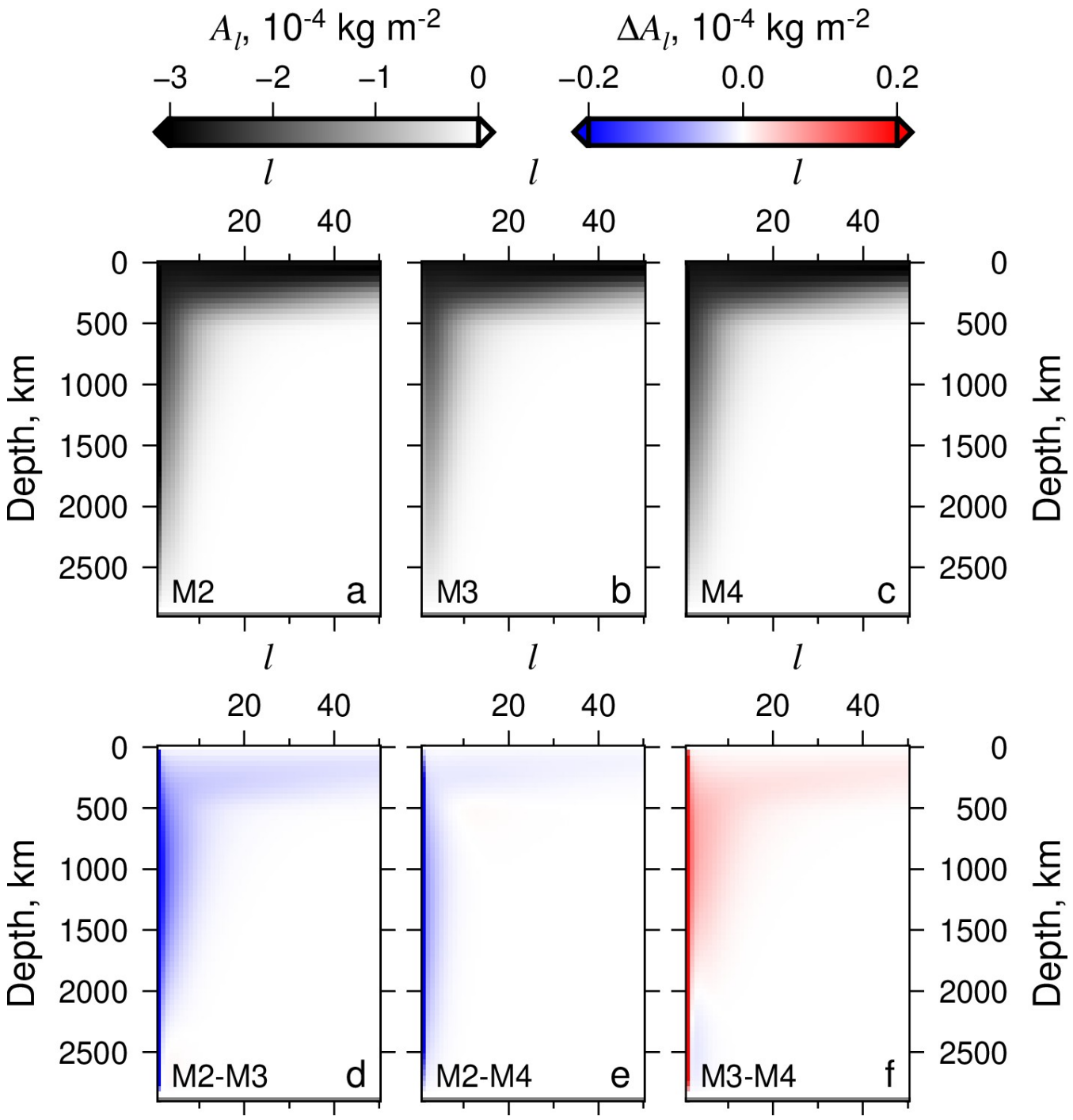

Figure S6. Comparison of sensitivity kernels generated with different treatment of gravitation. (a–c) Sensitivity kernels of Models 2 (M2; $g = 10$ m s^{-2}), 3 (M3; $g = g(r)$) and 4 (M4; gravitational potential of perturbed surface is included and $g = 10$ m s^{-2}); see Figures 3–4 & S3–S5. (d) Comparison of sensitivity kernels from Models 2 and 3; Model 3 kernel is subtracted from Model 2 kernel. (e–f) Comparisons of kernels from Models 2 & 4, and 3 & 4.

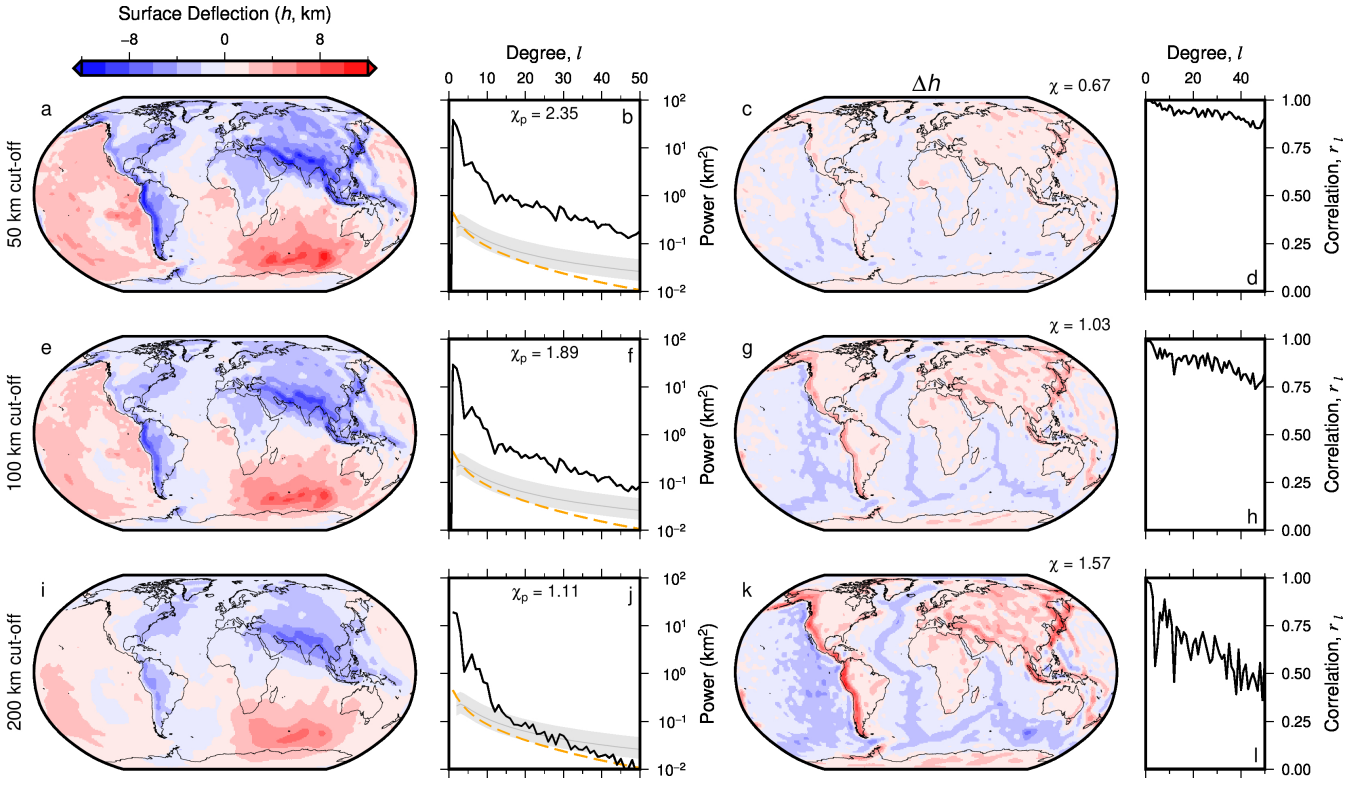

Figure S7. Models 5–7: Effect of removing shallow structure from analytic surface deflection calculations. (a) Model 5: Predicted water-loaded surface deflection from propagator matrix solution for Model 2, i.e., as Figure S3b, but with effect of upper 50 km of density anomaly structure ignored in calculation. (b) Black line = power spectrum of surface deflection shown in (a); gray line and band = expected dynamic topography from Kaula's rule using admittance $Z = 12 \pm 3$ mGal km^{-1} (Kaula, 1963). Orange dashed line = expected power spectrum for water-loaded residual topography from Holdt et al. (2022), via analytical solution of special case of Equation 4 in the main manuscript. $\chi_p =$ total root-mean-squared difference between distribution of modeled and theoretical surface deflection power (see Equation 9 in the main manuscript). (c) Difference between Models 5 and 2, i.e., between panel (a) and original propagator matrix solution, Model 2, shown in Figure S3b. (d) Spectral correlation coefficient, r_l, between Model 5 and 2; Equation 8 in the main manuscript. (e–h) and (i–l) as (a–d) but for depth cut-offs of 100 (Model 6) and 200 km (Model 7), respectively.

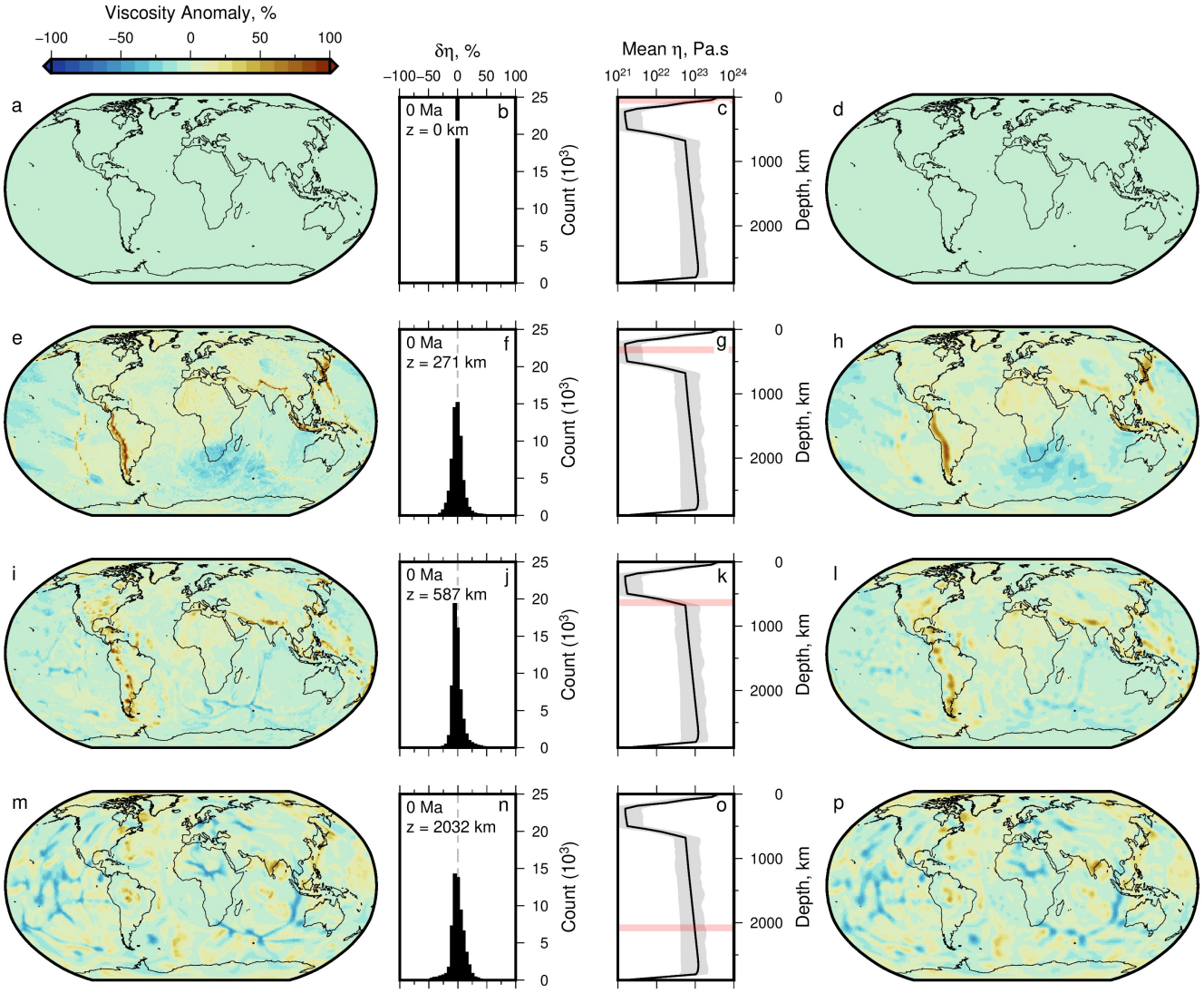

Figure S8. Model 11: Numerical simulation of mantle convection with temperature dependent viscosity, η, and spherical harmonic representation. (a) Present-day viscosity at surface from Model 11a, expressed as percentage deviation from layer mean, $\delta\eta$, plotted at grid resolution of 1 degree. (b) Histogram of values shown in (a), weighted by latitude to correct to equal-area. (c) Black line and gray band = global mean and extreme viscosity values as a function of depth; pink band = depth slice shown in (a). (d) Model 11b: Spherical harmonic fit up to degree l = 50 of grid shown in (a), using inverse approach of Hoggard et al. (2016). (e–h) As (a–d) but for depth slice at 271 km below surface. (i–l) and (m–p) 587 km and 2032 km depth slices.

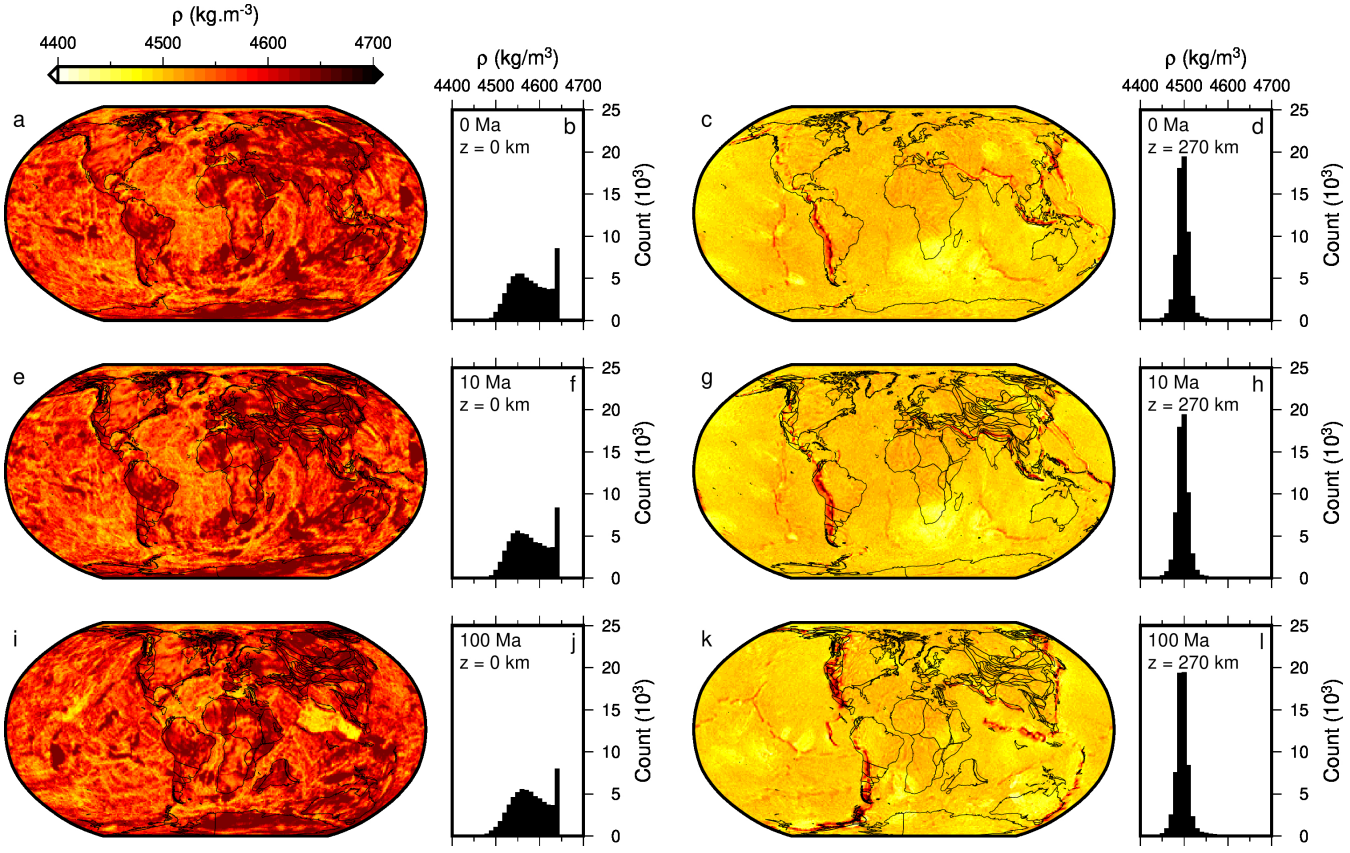

Figure S9. Model 11: Densities predicted by numerical simulation with temperature-dependent viscosity. (a) Predicted present-day density ρ, at surface (z=0), from TERRA model. (b) Histogram of values shown in (a), weighted by latitude. (c–d) As panels (a–b) but for densities at 270 km depth. (e–h) and (i–l) As panels (a–d) for time slices at 10 and 100 Ma (see caption of Figure S1 for expanded description; Figure S8 for viscosity structure; Equation S7 of this document).

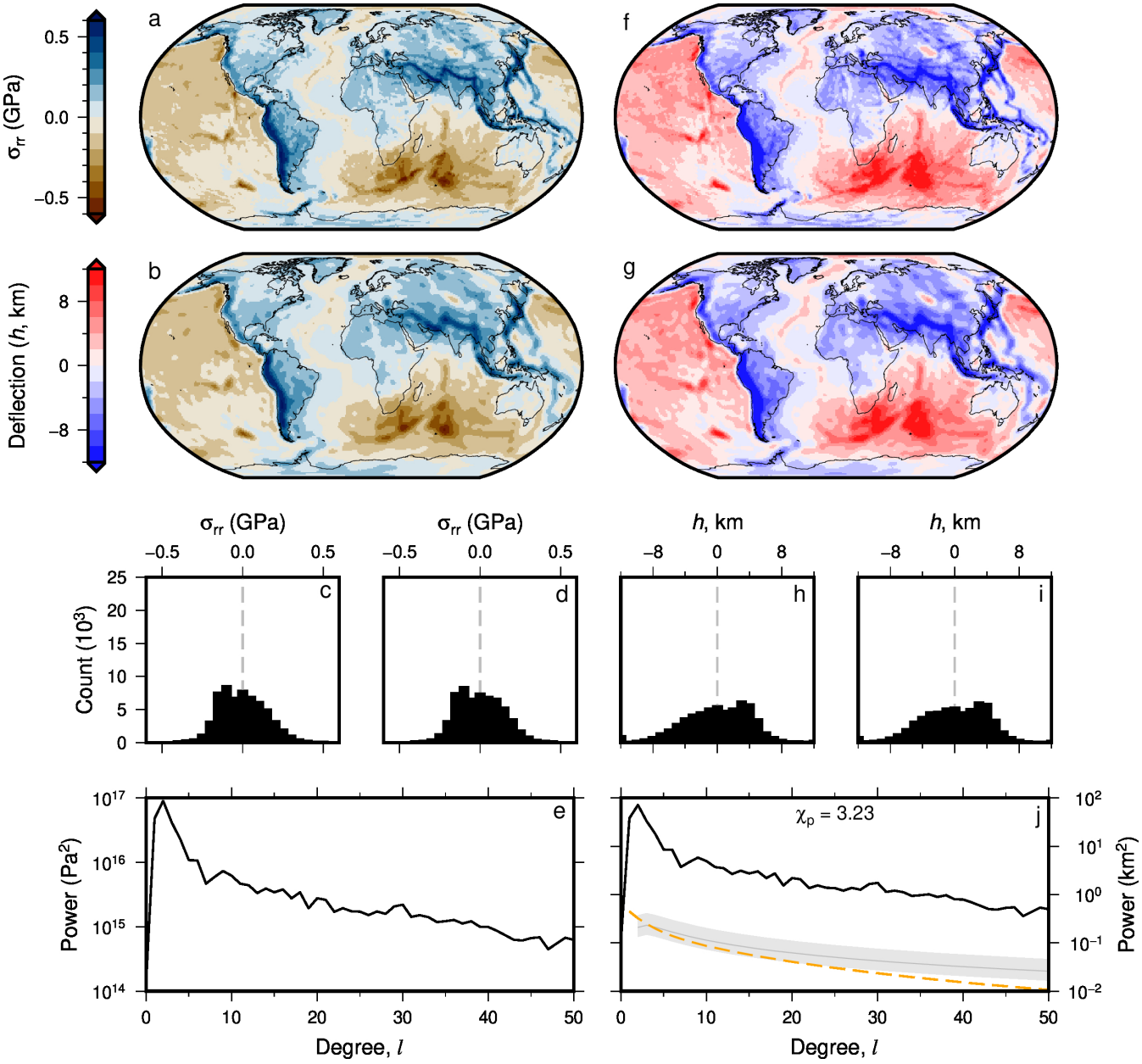

Figure S10. Model 11: Predictions of surface stresses and deflections from simulations with temperature dependent viscosity. (a) Predicted present-day surface radial stress, σ_{rr} from numerical TERRA model (Model 11a), plotted at grid resolution of 1 degree. (b) Model 11b: Spherical harmonic representation of Model 11a up to degree $l = 50$. (c) Histogram of values shown in (a), weighted by latitude to correct to equal-area. (d) Histogram of values shown in panel (b). (e) Power spectrum of surface stresses. (f–i) Calculated water-loaded surface deflections and associated histograms for full resolution numerical solutions (f, h) and spherical harmonic representation (g, i). (j) Power spectrum (black) of water-loaded surface deflection (panel g), Kaula's rule (grey curve and band), and water-loaded residual topography (orange); see Figure S2 for expanded description.

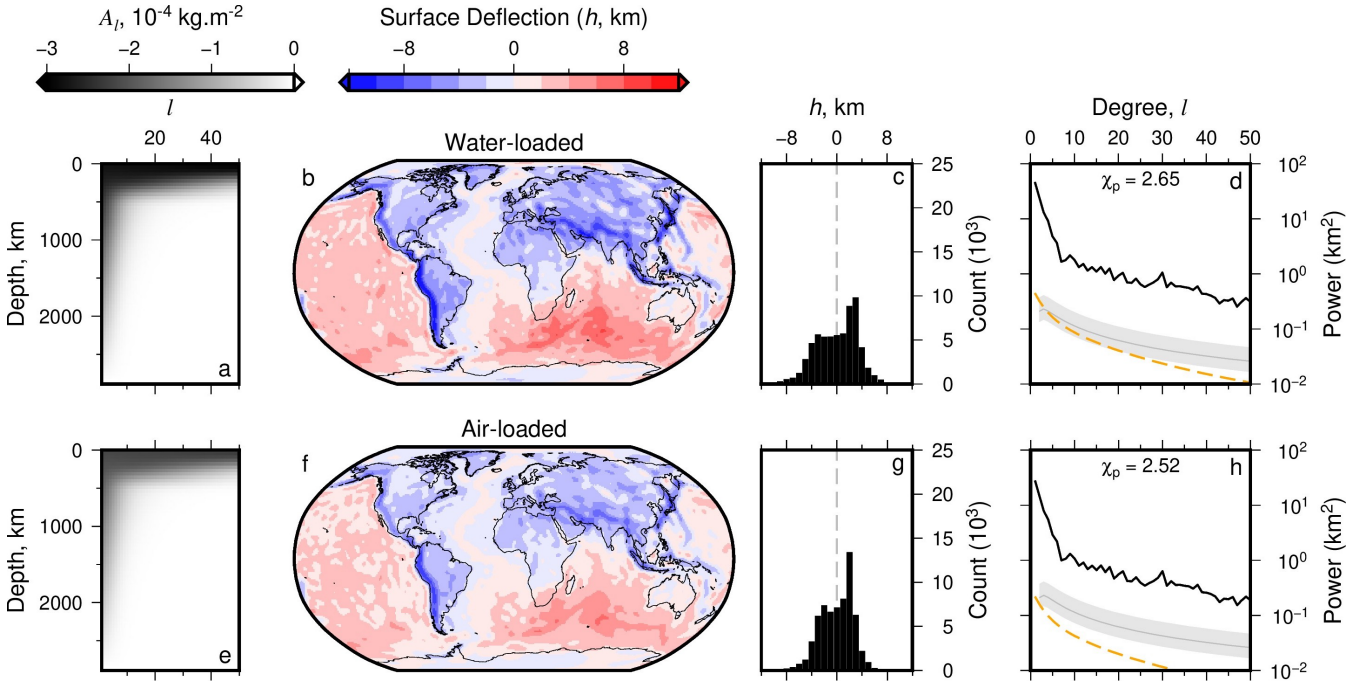

Figure S11. Model 12: Analytical (propagator matrix) predictions of surface deflections from simulations with temperature dependent viscosity. Radial viscosity is calculated using mean (radial) values from numerical model with temperature-dependent viscosity (i.e., Model 11a; Figure S10). (a–d) Present-day, water-loaded, surface deflection calculated analytically using propagator matrix solution; see Figure S3 for expanded description of panels. (e–h) Air-loaded deflection and associated metrics.

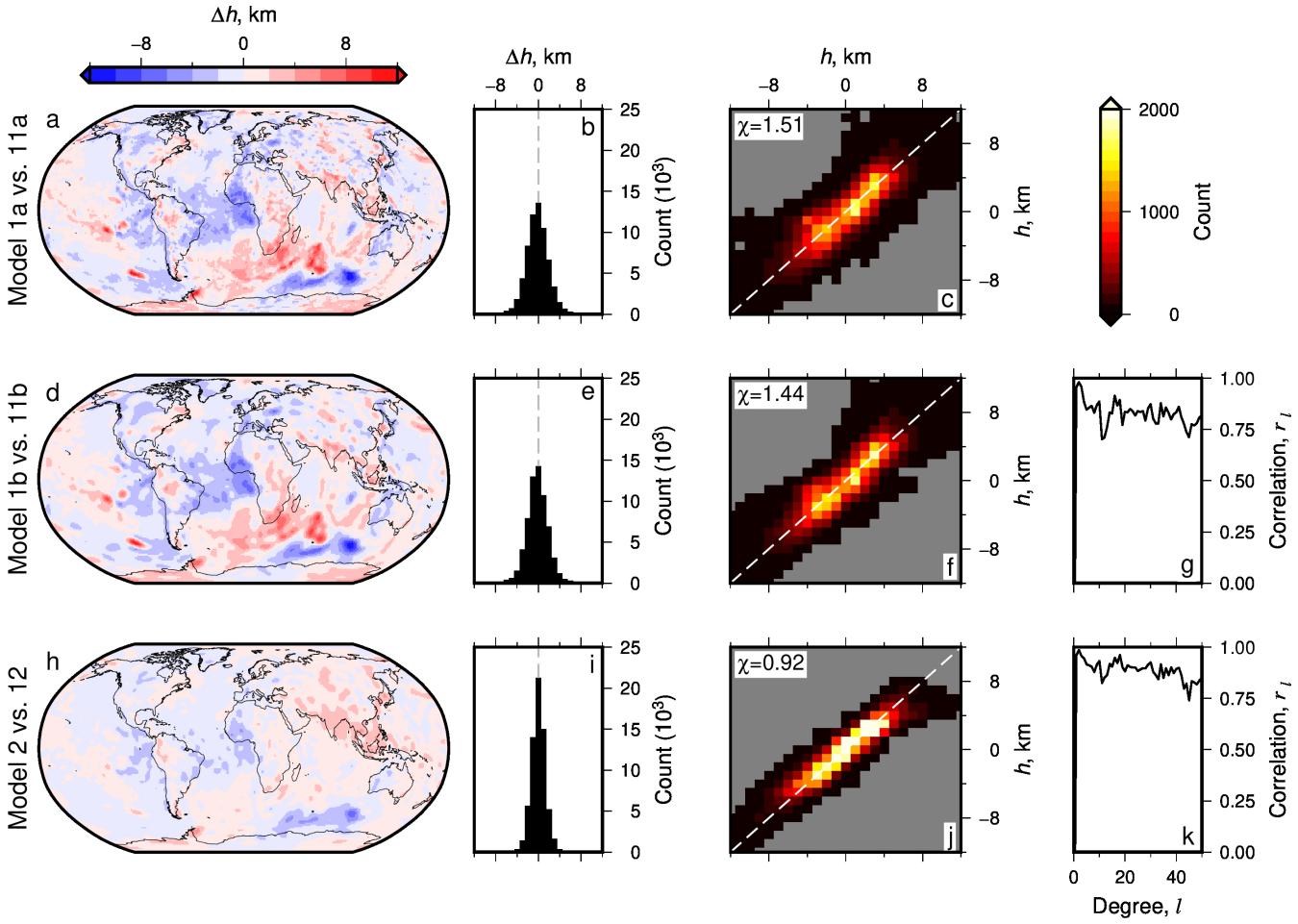

Figure S12. Comparing surface deflections calculated using normal stresses from numeric simulations (Models 1 and 11) and analytic estimates (Models 2 and 12) with and without temperature dependent viscosity. (a) Difference in predicted surface deflection, Δh, between numerical simulations with (Model 11a) and without (Model 1a) temperature-dependent viscosity. Full-resolution surface radial stresses are converted into surface deflections, h, using Equation 2 of the main manuscript. (b) Histogram of values shown in (a). (c) Pixel-wise comparison of predicted surface deflection between the two models; χ = root-mean-squared difference between predictions, see Equation 7 of the main manuscript; gray dashed line = 1:1 ratio. (d–f) as (a–c) but for surface deflection calculated using spherical harmonic expansion of surface radial stresses (Model 1b vs. 11b). (g) Spectral correlation coefficient, r_l, between model predictions (with and without temperature dependent viscosity; see Equation 8 of the main manuscript). (h–k) as (d–g) but for surface deflections calculated for each model using the propagator matrix approach (Model 2 vs. 12).

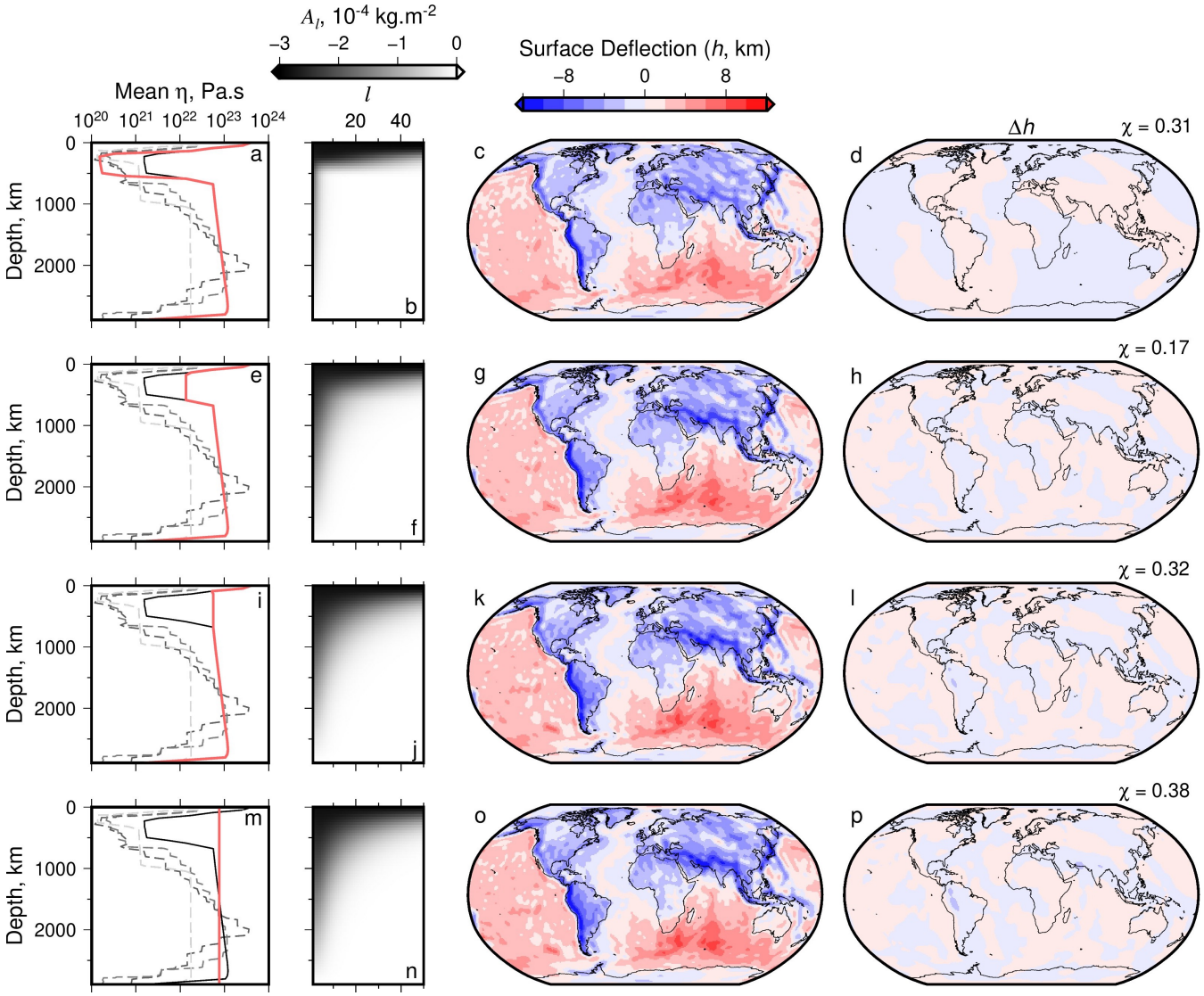

Figure S13. Models 13–16: Sensitivity of calculated analytic surface deflection to adjusted radial viscosity. (a) Model 13: Black curve = prediction of present-day radial mean viscosity from Model 11; red line = adjusted radial profile with viscosity decreased by a factor of 10 between depths of ∼ 300–500 km; gray dashed lines = viscosity profiles used in other studies (see Figure 2c). (b) Sensitivity kernel generated using adjusted viscosity shown in (a). (c) Surface deflection calculated using propagator matrix approach parameterised using adjusted viscosity profile (red curve in panel a), and resulting sensitivity kernel shown in panel (b). (d) Difference between propagator matrix solutions generated using adjusted and un-adjusted viscosity profiles, i.e., panel (c) minus Figure 7b (Model 13 vs. 12). Value of root-mean-squared difference, χ, (between calculated surface deflections for un-adjusted and adjusted viscosity) is stated (see Equation 7 of the main manuscript). (e–h) Model 14: As (a–d) but applying an increase in viscosity of a factor of 10 between ∼ 300–500 km. (i–l) Model 15: As (a–d) but applying an increase in viscosity of a factor of 100 between ∼ 300–500 km. (m–p) Model 16: As (a–d) but applying an constant viscosity of $\approx 7.5 \times 10^{22}$ Pa s (i.e., the mean value of the reference profile) across all depths.

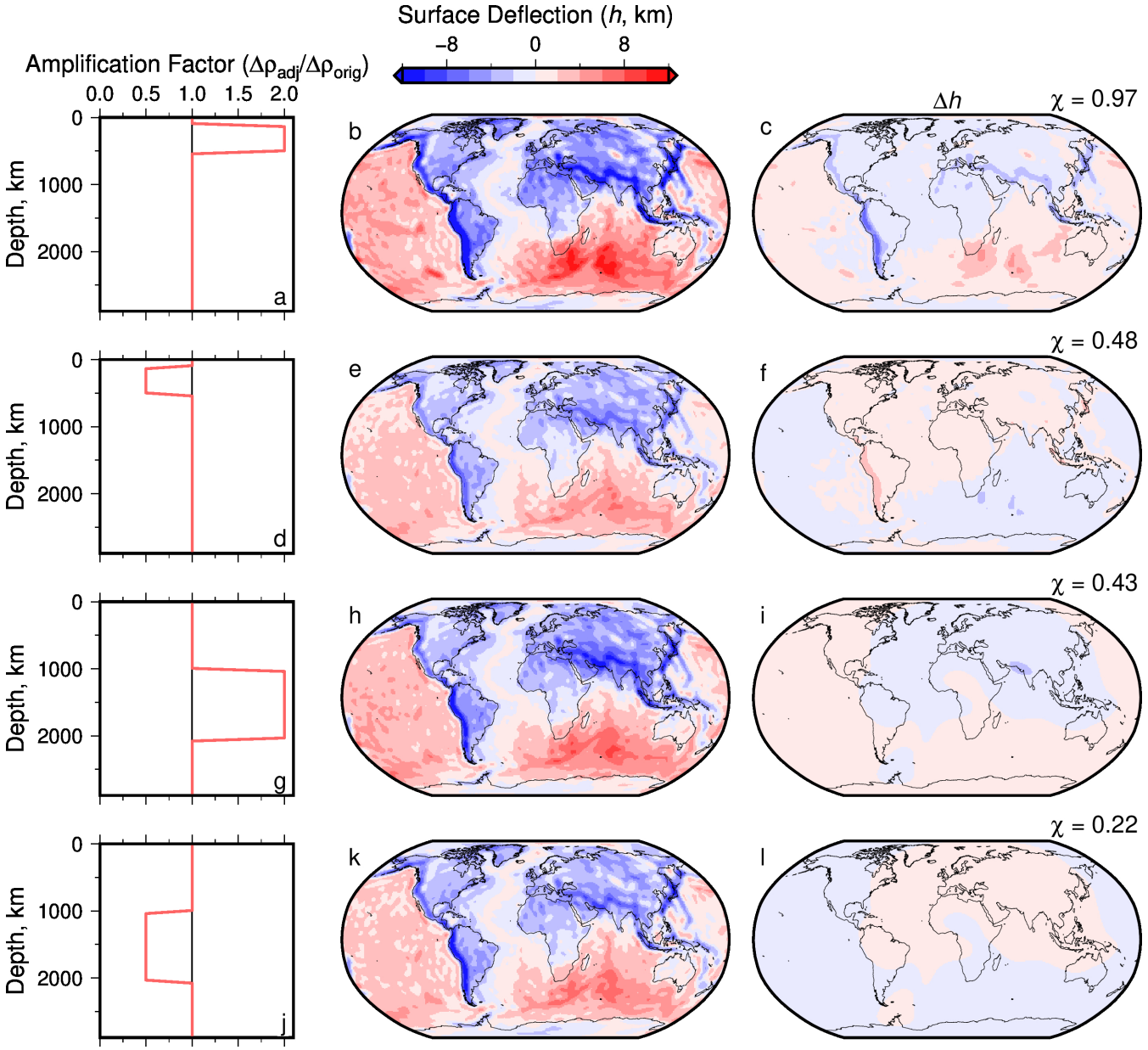

Figure S14. Models 17–20: Sensitivity of calculated analytic surface deflection to adjusted density anomalies. Annotation is as for Figure S13 but for adjusted density anomalies (red lines in left panels), by directly scaling spherical harmonic coefficients ($l > 0$) up or down by a factor of 2 (Models 17 & 19, panels a–c & g–i, respectively) or $\frac{1}{2}$ (Models 18 & 20: d–f & j–l). Viscosity structure applied in each case is same as that used to generate Figure 7b. Sensitivity kernels for surface deflection are not shown since they are invariant with respect to density anomalies, $\Delta\rho$, depending only on viscosity structure.

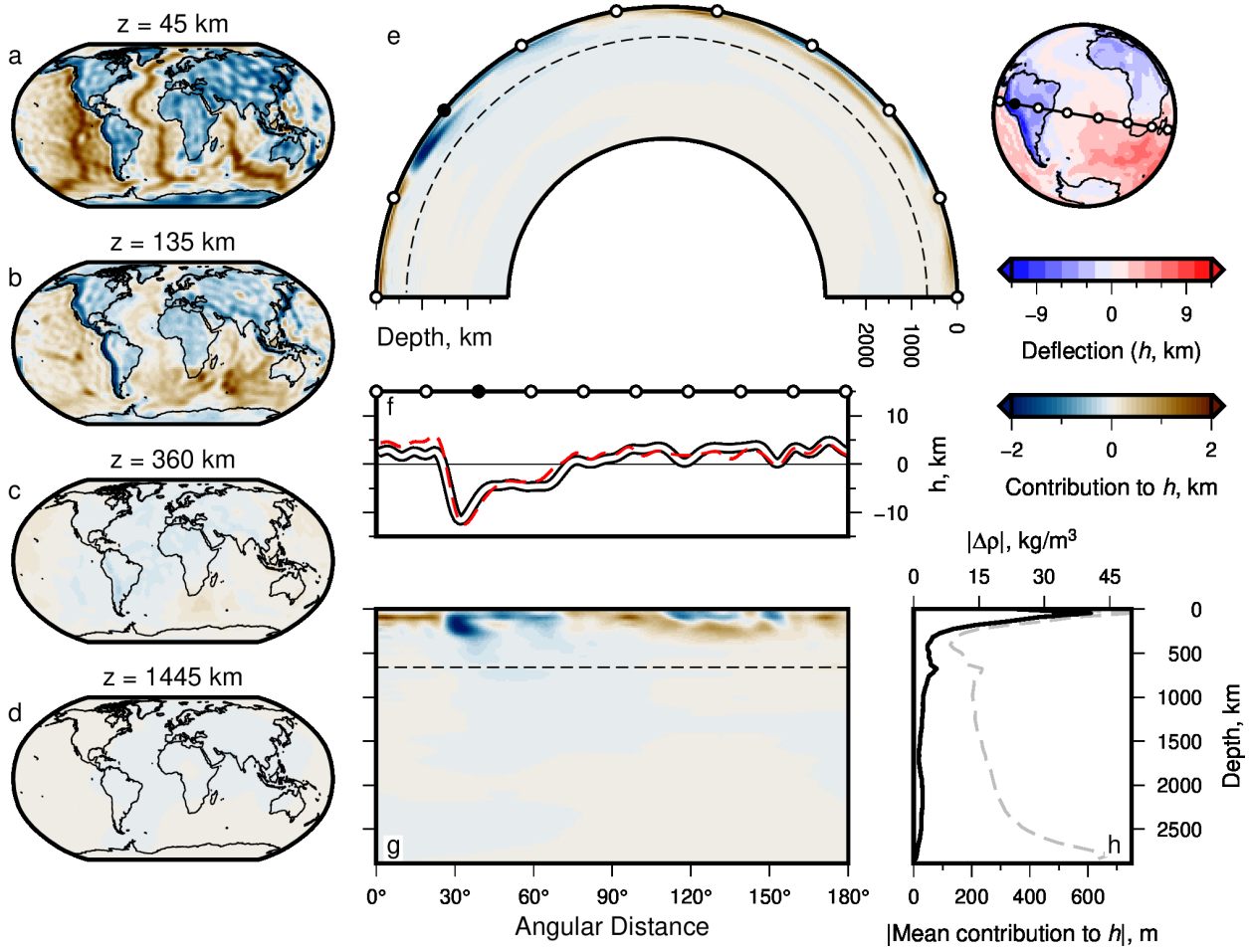

Figure S15. Surface deflections and effective densities up to maximum degree 40. (a–d) Net contribution to present-day water-loaded surface deflection calculated using analytical approach with maximum $l = 40$. Depth slices at 45, 135, 360 and 1445 km depth. (e) Great-circle slice (180°) showing contributions to surface deflection; globe to right shows transect location and calculated surface deflection, up to maximum $l = 40$. White circles = 20° intervals; filled black circle is for orientation; dashed line = 660 km depth contour. (f) White-black curve = surface deflection along transect shown atop globe in panel (e); red dashed curve = surface deflection from Model 2. (g) Cartesian version of panel (e). (h) Grey dashed curve = mean absolute value of density anomalies in Model 12—see top axis for values. Black curve = global mean amplitude (modulus) of contribution from density structure up to maximum $l = 40$ to total surface deflection h.

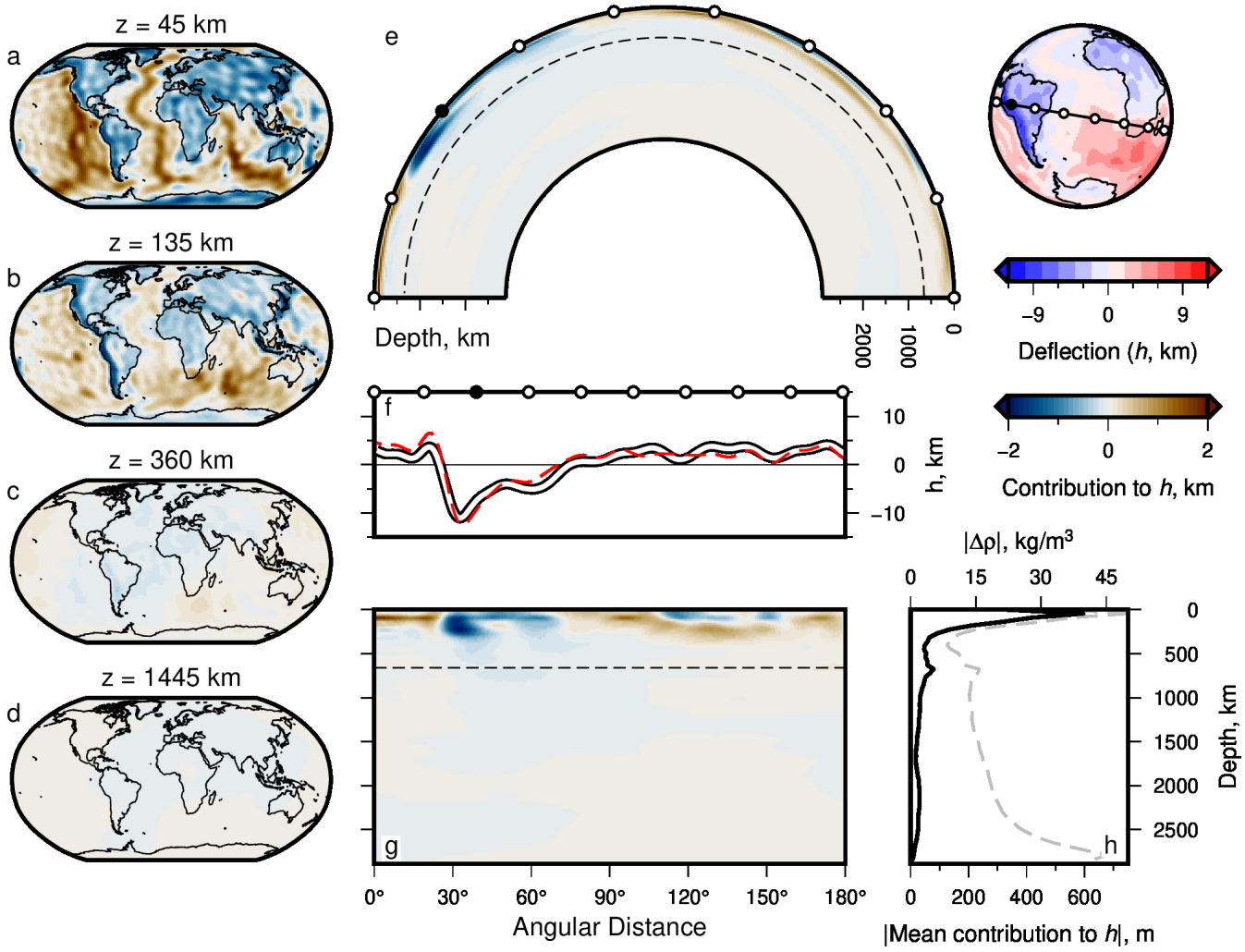

Figure S16. Surface deflections and effective densities up to maximum degree 30. As Figure S15, but for maximum spherical harmonic degree $l = 30$.

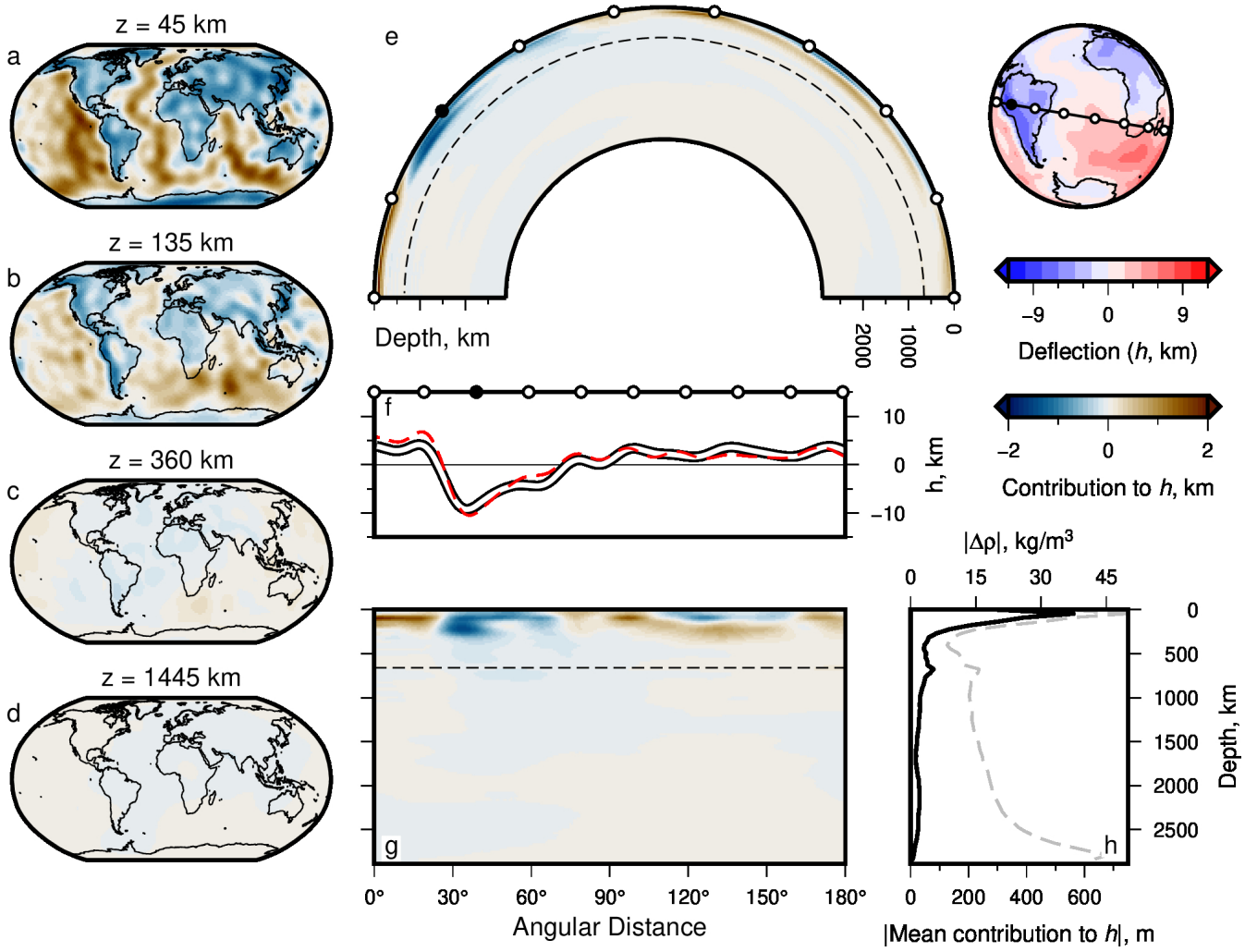

Figure S17. Surface deflections and effective densities up to maximum degree 20. As Figure S15, but for maximum spherical harmonic degree $l = 20$.

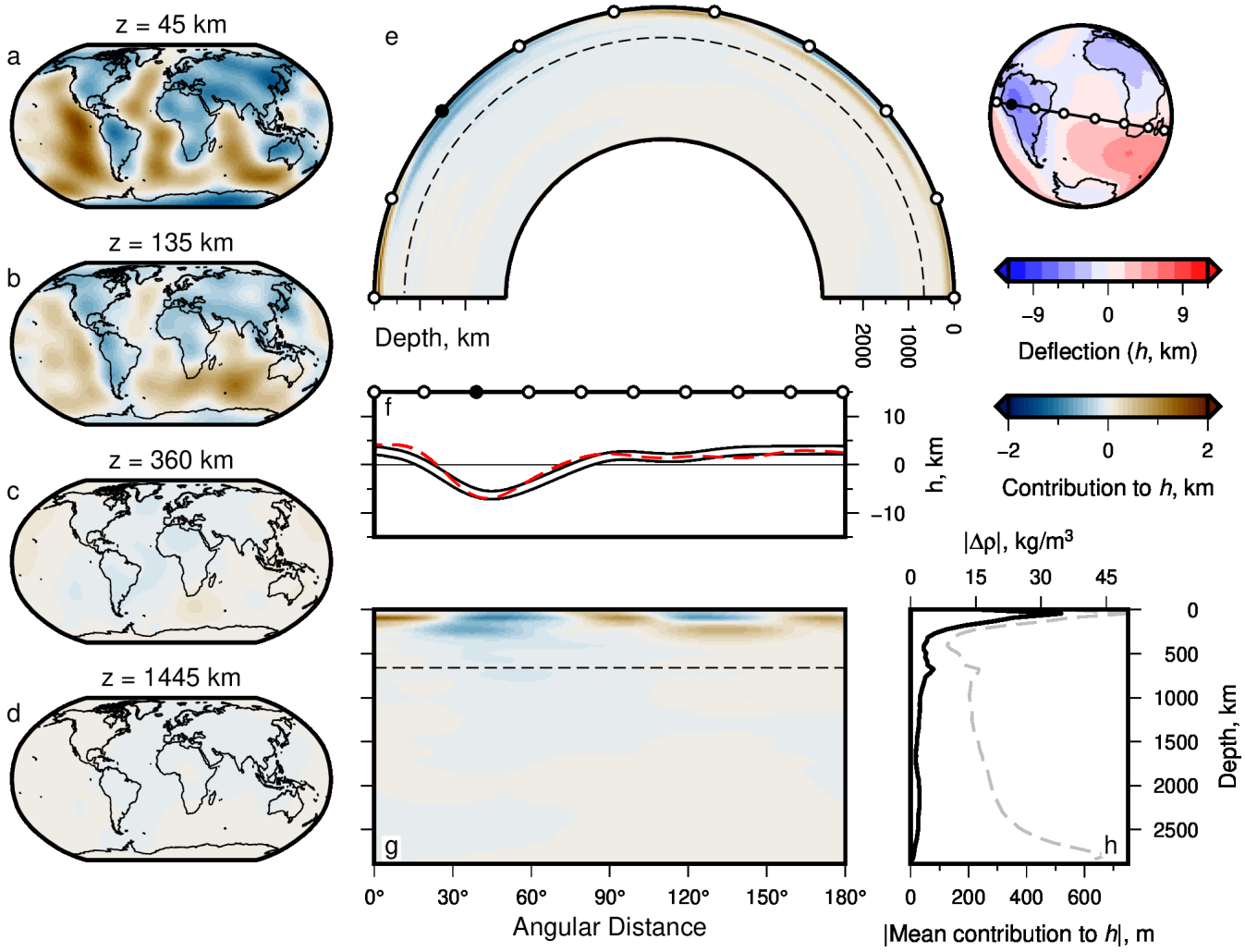

Figure S18. Surface deflections and effective densities up to maximum degree 10. As Figure S15, but for maximum spherical harmonic degree $l = 10$.

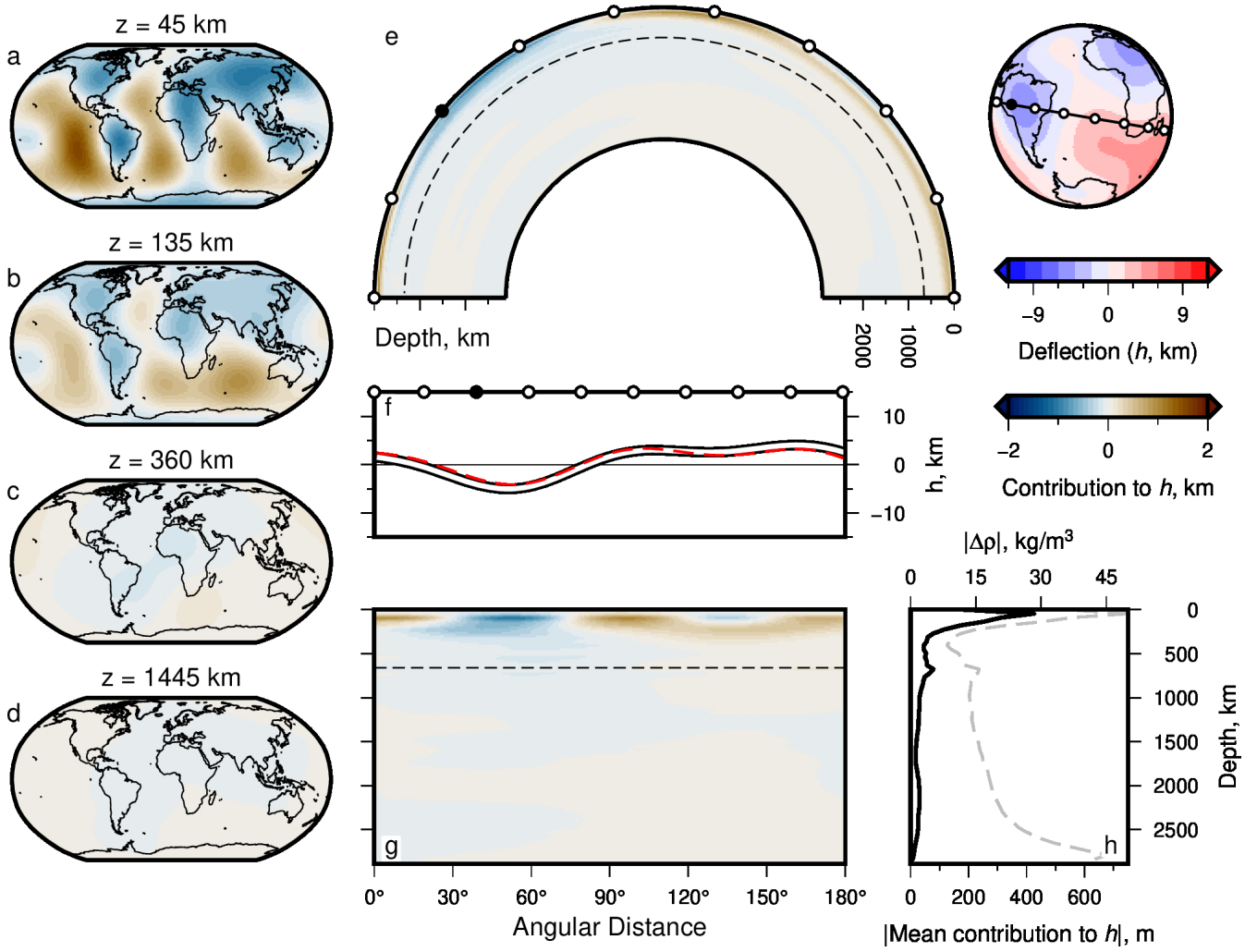

Figure S19. Surface deflections and effective densities up to maximum degree 5. As Figure S15, but for maximum spherical harmonic degree $l = 5$.